Quantification of capillary trapping of gas clusters using X-ray microtomography

Citation	Geistlinger, H., S. Mohammadian, S. Schlüter, and H.-J. Vogel (2014), Quantification of capillary trapping of gas clusters using X-ray microtomography. Water Resources Research, 50, 4514–4529. doi:10.1002/2013WR014657
DOI	10.1002/2013WR014657
Publisher	American Geophysical Union
Version	Version of Record
Terms of Use	http://cdss.library.oregonstate.edu/sa-termsofuse

AGU PUBLICATIONS

Water Resources Research

RESEARCH ARTICLE
10.1002/2013WR014657

Key Points:
- No systematic dependency of trapping efficiency on capillary number
- Majority of trapped gas bubbles (85%) are multipore trapped
- Trapping of gas clusters is determined by statistics and not by thermodynamics

Supporting Information:
- Supporting text, figures, and tables

Correspondence to:
H. Geistlinger,
helmut.geistlinger@ufz.de

Citation:
Geistlinger, H., S. Mohammadian, S. Schlueter, and H.-J. Vogel (2014), Quantification of capillary trapping of gas clusters using X-ray microtomography, *Water Resour. Res.*, *50*, 4514–4529, doi:10.1002/2013WR014657.

Received 27 AUG 2013
Accepted 25 APR 2014
Accepted article online 2 MAY 2014
Published online 30 MAY 2014

Quantification of capillary trapping of gas clusters using X-ray microtomography

Helmut Geistlinger[1], Sadjad Mohammadian[1], Steffen Schlueter[1,2], and Hans-Joerg Vogel[1]

[1]UFZ-Helmholtz Centre for Environmental Research, Halle, Germany, [2]Environmental Engineering, Oregon State University, Corvallis, Oregon, USA

Abstract A major difficulty in modeling multiphase flow in porous media is the emergence of trapped phases. Our experiments demonstrate that gas can be trapped in either single-pores, multipores, or in large connected networks. These large connected clusters can comprise up to eight grain volumes and can contain up to 50% of the whole trapped gas volume. About 85% of the gas volume is trapped by *multipore* gas clusters. This variety of possible trapped gas clusters of different shape and volume will lead to a better process understanding of bubble-mediated mass transfer. Since multipore gas bubbles are in contact with the solid surface through ultrathin adsorbed water films the interfacial area between trapped gas clusters and intergranular capillary water is only about 80% of the total gas surface. We could derive a significant ($R^2 = 0.98$) linear relationship between the gas-water-interface and gas saturation. We found no systematic dependency of the front velocity of the invading water phase in the velocity range from 0.1 to 0.6 cm/min corresponding to capillary numbers from 2×10^{-7} to 10^{-6}. Our experimental results indicate that the capillary trapping mechanism is controlled by the local pore structure and local connectivity and not by thermodynamics, i.e., by the minimum of the *Free Energy*, at least in the considered velocity range. Consistent with this physical picture is our finding that the trapping frequency (= bubble-size distribution) reflects the pore size distribution for the whole range of pore radii, i.e., the capillary trapping process is determined by statistics and not by thermodynamics.

1. Introduction

Capillary trapping of gas bubbles within water-saturated porous media, mobilization of trapped gas bubbles, and the dynamics of upward-moving gas bubbles play an important role in many processes in hydrogeology and soil physics. For CCS-technology (CCS—carbon capture and storage), capillary trapping is one of the relevant storage processes [*Iglauer et al*., 2011; *Juanes et al*., 2006]. For remediation of contaminated groundwater, gas sparging (oxygen) provides electron acceptors for biodegradation of organic contaminants by dissolving trapped oxygen gas bubbles [*McGray and Falta*, 1997; *Geistlinger et al*., 2009]. Noble gas tracer techniques are based on partition equilibrium between trapped gas bubbles and the surrounding water phase [*Holocher et al*., 2003]. For the highly transient transition zone (the capillary fringe) located between the unsaturated soil zone and near-surface groundwater, bubble entrapment and its dissolution controls the dissolved oxygen level and the activity of aerobic and anaerobic microorganisms, like nitrifiers or denitrifiers. The capillary fringe starts at the water table (water phase pressure corresponds to atmospheric pressure) and describes a region with higher water saturation as compared to the unsaturated zone due to capillary rise. In this region, usually water phase continuity is assumed, i.e., no isolated water drops exists. In contrast, the gas phase typically consists of isolated trapped gas phases or gas clusters and the interphase mass transfer is hindered by slow water diffusion. *Ronen et al*. [1989] studied the occurrence and the stability of a trapped gas bubble within the partially saturated capillary fringe. It was found that biologically mediated gas bubble formation, gas bubble growth, gas bubble dissolution, and gas bubble mobilization are governed by multicomponent mass transfer processes [*Ronen et al*., 1989; *Berkowitz et al*., 2004].

All described processes are governed by gas exchange from the water phase to gas phase and vice versa and are always driven by partial pressure gradients. The occurrence of stable trapped gas bubbles implies a vanishing steady state mass transfer rate, i.e., the dissolution rate has to be compensated by a mass transfer rate from the water phase into the gas bubble [*Ronen et al*., 1989]. Without a compensating mass transfer rate any trapped gas bubble will dissolve after few days in a typical groundwater environment, because of the capillary pressure that increases the partial pressure inside the gas bubble [*Geistlinger et al*., 2005]. The

key parameter that determines the mass transfer rate is the *gas-water interface*. An a priori knowledge of this important parameter for certain boundary conditions and for certain porous media is still a big challenge. Often lumped parameter models are used and the lumped parameter (the rate constant = mass transfer coefficient times *gas-water interface*) is used as a fitting parameter [*Powers et al*., 1991].

Direct measurements of two-fluid interfacial area are based on magnetic resonance imaging (entrapped gas bubbles) [*Ronen et al*., 1986], X-ray microtomography (μ-CT) [*Wildenschild and Sheppard*, 2013; *Werth et al*., 2010] ($scCO_2$-water interface [*Iglauer et al*., 2011]), scanning probe microscopy [*Wiesendanger*, 1994], and optical imaging [*Werth et al*., 2010; *Herman and Lemasters*, 1993]. Quantification of the fluid-fluid interface is often restricted to single cells containing two fluids or to 2-D micromodels of porous structures. For 3-D porous structures like sandstones μ-CT is used to analyze the surface distribution and the morphology of $scCO_2$-clusters [*Iglauer et al*., 2011; *Pentland et al*., 2012] and of oil and gas clusters, respectively [*Iglauer et al*., 2012, 2013].

Indirect methods for quantifying the interfacial area of two-fluid media are discussed by *Kibbey* [2013] and *Pan et al*. [2007].

Kibbey [2013] used Stereoscopic scanning electron microscopy to determine surface elevation maps of different surfaces with varying surface roughness. These surface maps were used as boundary condition to calculate the curvature of the gas-water interface by Young-Laplace equation. The results show that the configuration of surface-associated water is dominated by bridging of macroscopic surface roughness features over the range of the applied capillary pressure. For the limiting case of smooth surfaces (glass beads BG05 with a surface roughness of 267 nm) [see *Kibbey*, 2013, Table 1] and a capillary pressures of about 10 mbar, the mean value of the water film thickness was about 200 nm, i.e., 1 order of magnitude higher than the theoretical film thickness of adsorbed water films (10–20 nm) obtained by a DLVO model for flat surfaces [*Tokunaga*, 2011]. These calculations show that most of the surface-associated water is capillary-held water and not true adsorbed water. Since the water film will not follow the surface topology and the gas-water interface will bridge small cavities, microscopic surface roughness likely has minimal impact on the accuracy of surface-associated gas-water interfacial areas determined by limited resolution of μ-CT (e.g., 9 μm) [e.g., *Iglauer et al*., 2013].

Pan et al. [2007] applied a multiple-relaxation time lattice Boltzmann simulation to calculate the local flow field in random sphere packings and the dissolution of a generic residual NAPL-distribution. "Generic" means that the residual NAPL-morphology and NAPL-topology were simulated using a binary morphological approach [*Hilpert and Miller*, 2001]. This approach simulates quasi-static two-phase flow based upon size and connectivity of the digital pore space. The entrapped nonwetting NAPL-phase was quantitatively characterized by calculating (a) the NAPL-volume, (b) the NAPL-water interface, and (c) the different shapes of isolated NAPL-clusters. Since we characterize the trapped gas phase by the same measures, the comparison with this work is of special interest.

For the unsaturated soil zone, *Costanza-Robinson and Brusseau* [2002] classified model concepts with respect to their *water film contribution*. The first class only accounts for the capillary water in filled pores and pendular rings [*Gvirtzman and Roberts*, 1991; *Reeves and Celia*, 1996], and the second class accounts also for *water film contribution* [*Cary*, 1994; *Or and Tuller*, 1999; *Silverstein and Fort*, 2000; *Oostrom et al*., 2001]. *Or and Tuller* [1999] proposed a comprehensive unit cell of the porous media that is composed of a square-shaped central pore (for capillary-dominated processes) connected to slit-shaped spaces with internal surface area (for adsorption-dominated phenomena). The authors calculate the vapor-liquid interface as a sum of two contributions: (i) the contribution that is caused by capillary processes (curved menisci) and (ii) the contribution that is given by adsorbed water films. The augmented Young-Laplace equation was used to calculate the adsorbed water film area taking into account short-ranged ($\approx$10 nm) van der Waals interactions. In the dry-end limit of the unsaturated porous media ($S_w < 0.1$), the contribution of the ultrathin liquid films dominates the total vapor-liquid interfacial area. However, we are interested in the high-saturation limit ($S_w > 0.8$, mobile continuous wetting phase and discontinuous, trapped nonwetting phase, e.g., gas bubbles, NAPL-blobs, oil-blobs), where it is expected that adsorbed water films are not present. As *Or and Tuller* [1999] showed adsorbed water film contributions can be neglected above a critical water saturation of about 0.3 [see *Or and Tuller*, 1999, Figure 6a]. Mass transfer processes in multiphase flow at high saturation are determined by the contact area of the main flow paths of the mobile water phase with trapped

nonwetting phases, i.e., by the capillary-dominated interfacial area. The characterization of these contact areas is the objective of this paper.

In order to estimate the gas-water interface at the limit of high water saturation the characteristics of the trapped nonwetting phase, i.e., the morphology and topology of the trapped nonwetting phase clusters, must be known. *Pan et al*. [2007] showed this exemplarily for trapped NAPL-blobs. Because of its mathematical simplicity most authors estimate the gas-water interface based on the *standard model of gas bubble entrapment*. This model assumes that trapped gas bubbles or trapped gas clusters are completely surrounded by intergranular capillary-held water. (We use both terms to denote irregular shaped gas bubbles.) The absolute minimum of the *Free Energy* is given by the minimal gas-water interface. Hence, the standard model assumes that the wetting fluid resides preferably in smaller pores, so that the size distribution of entrapped gas corresponds to the larger pores as shown in Figure 12. This will be referred to as "thermodynamical filling," i.e., bubble-size distribution and pore size distribution are not correlated over the whole range of pore radii.

To our knowledge, all papers on gas bubble entrapment or bubbly and channelized gas flow in saturated porous media inherently assume complete wetting by thick water films and/or intergranular capillary-held water, and single-pore trapped gas bubbles or single-pore gas channels. *Holocher et al*. [2003] and *Oswald et al*. [2008] consider complete wetting and uniform bubble distribution (equal sized; four bubble classes); in their pioneering paper *Brooks et al*. [1999] consider the onset of bubbly gas movement based on the assumption of single-pore trapped gas bubbles which has now been disproven; *Ezeuko and McDougall* [2010] used the single-bubble mobility criterion in order to generate network models for discontinuous (= incoherent) bubbly flow; *Roy and Smith* [2007] studied the formation and growth of single trapped gas bubbles, which are spontaneously formed above a DNAPL (PCE-phase); *Enouy et al*. [2011] developed a remediation technology based on exsolution of CO_2-gas bubbles from supersaturated water (SWI-technology); *Geistlinger et al*. [2005] investigated experimentally the dissolution behavior of trapped gas bubble; *Fry et al*. [1997] conduct a comprehensive study on the capillary trapping efficiency of different gas injection methods; *Donaldson et al*. [1997] derived a mass transfer coefficient for the dissolution of trapped gas bubbles. Furthermore, all visualization studies on air sparging with transparent columns or 2-D plexiglas modules filled with glass beads or natural sands [e.g., *Glass et al*., 2000; *Selker et al*., 2007; *Geistlinger et al*., 2009] are based on the complete-wetting assumption: the gas channels are considered as connected gas clusters through complete wetted glass beads or sand grains. On this basis, the capillary forces, viscous forces, and buoyant forces are compared and calculated [see, e.g., *Glass et al*., 2000].

The present study focuses on bubble entrapment within the capillary fringe due to water table rise. Our *working hypothesis* is: the faster the water table rises, the more gas will be trapped. Since this is derived from the fact that the porous system needs a so-called relaxation time to establish the thermodynamic equilibrium, what means to minimize its *Free Energy* (minimal interface = minimal gas bubble trapping efficiency). The following questions will be studied: (i) is a gas bubble always trapped within a single macropore or are multipore trapped gas bubbles possible, too? (ii) What is the correlation between the bubble-size and pore size distribution? (iii) Are the filling of the pores determined by thermodynamics, i.e., by the absolute minimum of the *Free Energy* and hence macropores are filled first, or by kinetics, i.e., fast water imbibition determines the capillary trapping of gas clusters? Answering these critical questions will provide new insight to the reviewed processes of capillary trapping and bubbly gas flow. This study will serve to improve theoretical estimates for the bubble-mediated mass transfer that is included in multiphase flow simulations at larger scales.

In the current study, we used X-ray microcomputer tomography to *directly* measure the gas-water interface in unsaturated glass beads (diameter 1 mm). Based on image processing, we were able to quantify (a) the gas phase volume, (b) the gas-water interface, and (c) the different shapes of isolated gas clusters. The paper is organized as follows: based on the standard model the geometry of a single-pore trapped gas bubble is discussed in section 2 and compared with the experimental geometry obtained from a high-resolution CT-image. In section 3, we describe the μ-CT-experiments and the image processing for quantification of the gas phase distribution. In section 4, we present the results and discuss their implications.

2. Standard Model for Gas-Bubble Entrapment and Comparison With Experiments

There are main differences of the trapping behavior of nonwetting phases between strongly water-wet (air-water) and weaker water-wet three-phase systems (NAPL-water, $scCO_2$-brine, oil-water) for porous media like

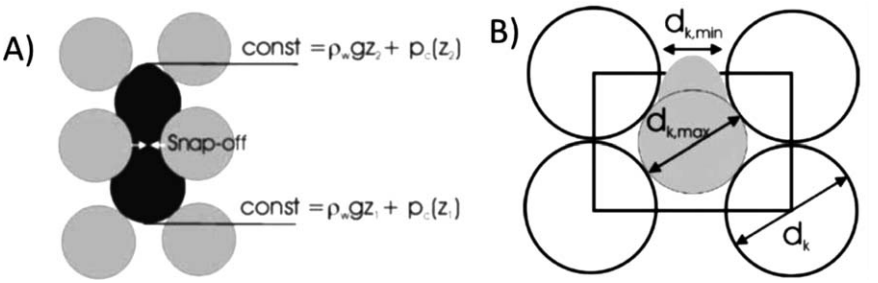

Figure 1. Standard model of gas bubble entrapment: (a) unstable large gas clusters will split into smaller ones. (b) Single-pore trapped gas bubble (gray) in simple-cubic coordinated glass beads. The rectangle represents the diagonal cross section through the unit cell.

glass beads or sandstones: (i) *Contact angle* [see *Iglauer et al.*, 2011; *Blunt and Scher*, 1995]: the amount of trapping depends on the fluid-fluid displacement mechanism. There is a competition between piston-like displacement and core-annular displacement [see *Joseph and Renardy*, 1993; *Dullien*, 1992]. In a strongly water-wet porous medium (contact angle close to zero), water flows along the walls in thick wetting layers (annular flow). During imbibition these layers swell, leading to snap-off at narrow pore necks. Curved interfaces due to geometrical configuration, surface roughness, and thermodynamical fluctuations lead often to instability [*Joseph and Renardy*, 1993; *Dullien*, 1992]. As the contact angle increases (NAPL [*Pan et al.*, 2007]; $scCO_2$ [*Iglauer et al.*, 2011]; oil [*Berg et al.*, 2013], oil-gas-water: mixed wettability through oil-gas-brine flood sequences [*Iglauer et al.*, 2013]) snap-off is less favored and the dominant mode of displacement is cooperative piston-like flow [*Iglauer et al.*, 2011]. (ii) *Surface tension/viscosity*: in case of core-annular flow the thick convex-curved water films become unstable and are driven by the interface tension, i.e., as larger the interface tension as faster snap-off occurs (fastest growing unstable mode depends exponentially on surface tension, for details of linear stability analysis see *Joseph and Renardy* [1993]; interface tension in mN/m: air-water = 73, $scCO_2$-brine = 36 [*Chalbaud et al.*, 2009], oil-water = 35 [*Berg et al.*, 2013], Toluene-water = 28.5 [*Pan et al.*, 2007]). The resistance forces against snap-off are friction forces and acceleration forces which are controlled by fluid viscosity and density. In case of an oil-water system, the viscosity of the oil phase leads to a slower snap-off-process compared to a gas-water system. Experimental evidence for the weaker snap-off tendency in $scCO_2$-brine or oil-water three phase systems is the observed large multipore clusters [*Berg et al.*, 2013; *Iglauer et al.*, 2011, 2013] or NAPL-ganglia [*Pan et al.*, 2007; *Powers et al.*, 1991]. Such large multipore trapped gas bubbles are not expected in strongly water-wet systems. Therefore, a common and reasonable assumption is that large coherent gas clusters are unstable and that snap-off events will lead to single-pore trapped bubbles as shown in Figure 1a (for details see supporting information Text S1 and *Geistlinger et al.* [2006]).

The wetting behavior of glass beads (contact angles lie in a typical range between 10° and 30°; acetone-cleaned or H_2O_2-cleaned glass < 10°; water-rinsed glass: 25°; untreated glass: 32°) [*Sumner et al.*, 2004] prevents larger bubble diameters than $d_{k,max}$ (= maximal pore diameter), which guarantees that the glass beads are always surrounded by the water phase; at least by a thick water film. The curvature at the top (z_2) of a single-pore trapped gas bubble has to be larger than that at the bottom (z_1) of the gas bubble (Figure 1a), i.e., the higher hydrostatic pressure at the bottom leads to a smaller capillary pressure, since the gas pressure over the whole gas bubble has to be constant (see also supporting information Text S1). Based on this single-pore entrapment process a quasi-static mobility criterion [*Brooks et al.*, 1999; *Ezeuko and McDougall*, 2010] can be derived assuming mechanical equilibrium between capillary and buoyancy forces. Usually, this results in a critical radius or a critical gas cluster length of 3–4 mm. Consequently, single-pore trapped gas bubbles never become mobile in glass beads with a pore diameter smaller than 3 mm what means a grain diameter, d_k, of about 5 mm ($\xi_{max} = d_{k,max}/d_k$, $d_{k,max}$ is the maximal pore diameter, $\xi_{max} \cong 0.60$; this holds for 0.5, 1, and 2 mm-glass beads sediments (= GBS); packing density 1.51 g/cm^3, porosity 0.36–0.39) [for details, see *Geistlinger et al.*, 2006]. Furthermore, gas clusters with a length of several grain diameters become unstable as discussed above. Both findings are in contradiction with experimental results. As shown in *Geistlinger et al.* [2006, 2009] gas bubbles become mobile already in 2 mm glass beads and gas cluster length of several grain diameters were observed. In various experiments on gas flow in water-saturated glass beads, we often observed that trapped gas bubbles are in contact with the grains, i.e., water films were not visible.

In order to solve this contradiction and to understand the trapping mechanism of a nonwetting phase (gas, oil, NAPL), we consider the geometrical form of a single-pore trapped gas bubble with a radius larger than

the critical radius $r_b = r_{k,max} = d_{k,max}/2$, Figure 2a) shows a trapped gas bubble with the critical radius in 2-D and 3-D that is completely surrounded by intergranular capillary-held water. What happens, if the bubble radius exceeds the critical radius (Figure 2b, $r_b = d_k/2$)? Will the thick water film along the dashed line within the overlapping section lead to instability and snap-off of this large bubble into two smaller ones or is a new stable bubble configuration thermodynamically possible? The thermodynamical treatment of these two cases is provided in the supporting information Text S1, here we will only discuss the results: (i) If there exists a thick water film, then a trapped gas bubble with $r_b > r_{k,max}$ is thermodynamically *unstable*, because of the convex, negative curvature ($-1/r_k$) of the dashed line section. This negative curvature has to be compensated by a higher positive curvature (higher capillary pressure) around the bubble neck. Hence, the bubble neck will thin and snap-off will occur. This is the standard snap-off argument used in literature [see *Dullien*, 1992, p. 430]. (ii) If there exists a *stable* trapped gas bubble with $r_b > r_{k,max}$ with a thick water film along the dashed line section then an additional repulsive or disjoining pressure is needed to compensate the negative capillary pressure caused by the convex curvature. *Kovscek et al*. [1993] discussed this case based on the augmented Young-Laplace equation and showed that the convex contact areas shown in Figure 2b are important to elucidate wettability properties on the pore level. The augmented Young-Laplace equation takes into account a short-ranged (nm scale) disjoining or Derjaguin pressure [*Derjaguin*, 1940]. The disjoining pressure contains three major force components: hydration forces, van der Waals forces, and electrical-double layer forces. A typical disjoining pressure isotherm is shown in Figure 3 for the case of a trapped gas bubble (dashed line) and oil-blob or NAPL-blob, respectively (solid line). We note that a general treatment of the disjoining pressure isotherm goes beyond the scope of this paper and can be found in *Verwey and Overbeck* [1948], *Melrose* [1982], *Safran* [1994], *Radoev et al*. [2007], and *Tokunaga* [2011]. Here we discuss only the qualitative features of the disjoining pressure isotherm following *Kovscek et al*. [1993]. The force balance of a thin adsorbed water film is established at a thickness h(gas) of about 12 nm (see Figure 3) and a disjoining pressure of about 400 Pa, where we have calculated the disjoining pressure by the repulsive van der Waals forces [*Or and Tuller*, 1999] and using a Hamaker constant of -1.3×10^{-20} J (air-water-SiO_2, *French*, 2000; see supporting information Text S1). In case of a trapped oil- or NAPL-blob, a further reduction of the film thickness is possible due to attractive van der Waals forces. If the curvature of the oil-water interface exceeds a critical value, i.e., the maximal disjoining pressure Π_{max}, then the thin water film becomes unstable and a new stable interface is established at a film thickness of few monolayers denoted by h(oil) in Figure 3. As discussed by *Kvoscek et al*. [1993] and *Blunt* [2001] these ultrathin adsorbed water films are regions of high mass transfer between the adsorbed polar molecules and the polar components of the nonwetting phase and will change the composition of the adsorbate, i.e., the wetting properties of the solid surface.

From the capillary analysis of glass bead packings two important conclusions can be drawn: (i) The gas-water interface is given by the sum of the surface-associated area of thin adsorbed water films and the intergranular capillary area. Because of the limited resolution of the μ-CT (25–85 μm) only the intergranular capillary area will be measured. (ii) Convex-curved gas bubbles are a strong indicator for thin adsorbed water films that are represented by the dashed lines within the overlapping section in Figure 2b. In Figure 2b, a 3-D gas bubble with convex curvature and spherical geometry is shown that satisfies the thermodynamic condition, namely that the apparent contact angle has to be constant ($= 60^\circ$; exact result) along the apparent three-phase boundary [for the definition of the apparent contact angle and apparent three-phase boundary in the presence of thin adsorbed water films, see *Wong et al*., 1992]. For a three-phase-system with a simple-cubic pore structure and an apparent contact angle of 60° of the wetting fluid Figure 2b shows the correct bubble shape. For smaller apparent contact angles, e.g., 10° for the wetting fluid water, the shape is determined by the condition that the curvature is constant along the gas-water interface, because of constant gas pressure inside the gas bubble. Since the curvature is given by the sum over the principal directions, i.e., $1/r_1 + 1/r_2$, the higher curvature in vertical direction at the apparent three-phase boundary will be compensated by a smaller curvature along the horizontal direction. Merging to the top of the bubble both curvatures become equal, because of symmetry, i.e., it holds: $2/r_3 = 1/r_1 + 1/r_2$, with $r_1 < r_3 < r_2$. For the general case ($\theta \neq 60^\circ$; bubble radius $r_b \neq r_k$) the geometrical form has to be calculated by means of differential geometry under the constraint of a minimal gas-water interface with constant curvature (constant gas pressure). The 3-D gas bubble with spherical geometry is an idealized model of a realistic trapped gas bubble shown in Figure 4 that exhibits the following important features: (i) surface-associated interface areas with convex curvature, (ii) the existence of apparent three-phase boundaries, (iii) a constant

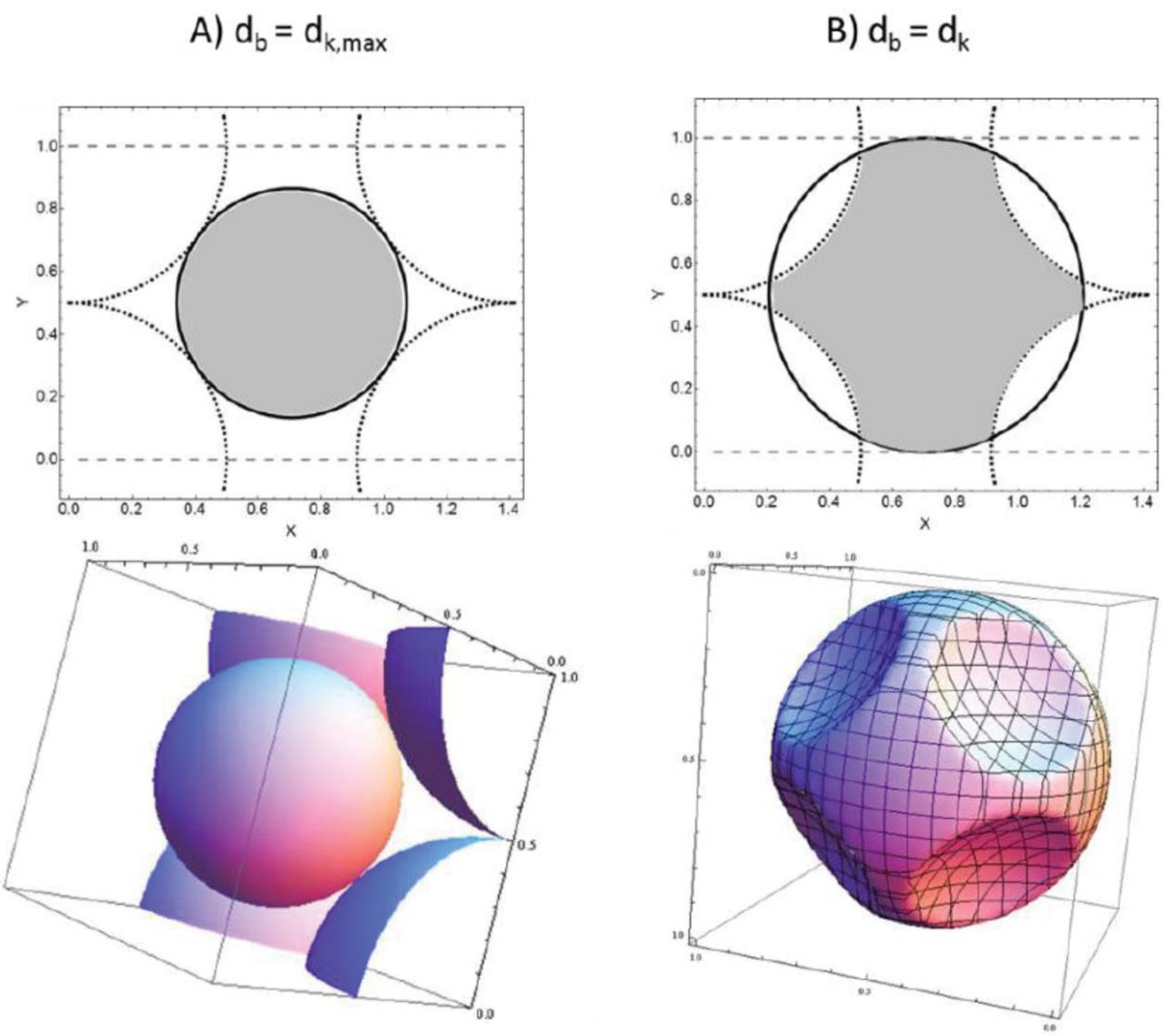

Figure 2. Trapped gas bubble within a cubic unit cell: (a) bubble diameter $d_b = d_{k,max}$ and (b) bubble diameter is equal to the grain diameter d_k. (top row) The 2-D representation of a trapped gas bubble (gray area).

apparent contact angle along the apparent three-phase boundaries, and (iv) a constant curvature for the gas-water menisci.

As shown in Figure 4, we indeed observed such trapped gas bubbles with convex curvatures. The spatial resolution of the CT-image is 25 μm. Figure 4 shows a horizontal cut through a trapped gas bubble (flat upper surface), in order to visualize the convex curvature of the trapped gas bubble and its similarity to the theoretical gas bubble shown in Figure 2b. The experimental trapped gas bubble exhibits five convex curvatures indicating gas-solid interfaces separated by thin adsorbed water films. Note that the theoretical bubble exhibits only four convex-curved interfaces for a horizontal cut, because it was based on a simple-cubic environment with six nearest neighbors. The experimental configuration is always higher and lies between 6 and 12. An unexpected result was the existence of such surface-associated areas of thin adsorbed water films in the high-saturation limit ($S_w > 0.8$), where one anticipates only intergranular capillary area. From the stability argument discussed in the supporting information Text S1, we conclude that these surface-associated areas are thin adsorbed water films [*Kvoscek et al*., 1993; *Tokunaga*, 2011]. However, as *Kibbey* [2013] has shown, true adsorbed films may be rare, because of surface roughness. Thus one would expect a film thickness of about 200 nm for smooth glass beads and capillary pressures in the range between 4 and 10 mbar. This could explain our experimental observations of no visible water films in gas injection experiments.

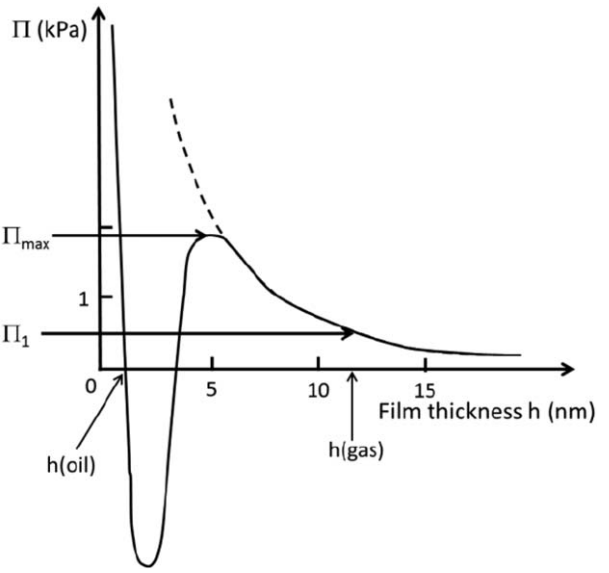

Figure 3. Disjoining pressure isotherm for water films on silica surfaces in presence of a trapped nonwetting phase (gas: dashed line, oil: solid line, $\Pi_1 \cong 0.4$ kPa).

3. CT-Experiments and Image Processing

3.1. Experimental Setup

A column of 30 cm length and an inner diameter of 3.18 cm was filled with 1 mm glass beads ($d_{50} = 0.85$ mm, $d_{10} = 1$ mm, $d_{95} = 0.8$ mm). Prior to packing, the glass beads were cleaned with acetone and water and dried at 105°C. To achieve a close, reproducible packing, small vibrations to the column were applied during the continuous filling process. The packing density of regular, equal-sized glass beads can vary between the loosest cubic packing (coordination number 6, porosity $\phi = 0.4764$) and the densest, cubic-face-centered packing (coordination number 12, porosity $\phi = 0.2595$) [*Dullien*, 1992]. All packed columns exhibit close random packing resulting in a porosity of 0.332 ± 0.005 (packing density = 1.61 kg/L, particle density = 2.41 kg/L). Before saturating the column with water the column was flushed with CO_2-gas to ensure that any trapped gas phase will dissolve rapidly. The column was then saturated with water to a certain position z_0 that was measured with a bypass capillary (diameter = 5 mm). This bypass capillary was necessary for measuring the water table, because of the roughness of the capillary fringe (about 1 cm). Since we have increased the water table within the column nearly quasi static, we assume that no gas bubbles are trapped and the initial water saturation below z_0 is zero. To prove this, we evaluate the volumetric gas content by μ-CT and found a value smaller than 1%. The initial state was prepared prior each new experiment. Starting from the initial state we increase the water table to $z_1 = z_0 + 5$ cm with a certain water table rising velocity of 0.1, 0.2, 0.3, 0.4, 0.5, and 0.6 cm/min. These rising velocities corresponds to capillary numbers between 2×10^{-7} and 10^{-6} and are far too high for typical groundwater level fluctuations in agricultural areas [*Geistlinger et al.*, 2010]. These velocities may be comparable with groundwater level fluctuations in irrigation areas or at groundwater-river interfaces. We note that the capillary numbers are comparable to $scCO_2$-injection into brine saturated sandstone cores (10^{-6} [*Iglauer et al.*, 2011]) and to brine flooding of oil-gas-saturated sandstone cores (10^{-6} [*Iglauer et al.*, 2013]). To estimate the influence of a varying local pore structure, we conducted three experiments each was repacked prior to the experiment and then the same water table rise velocity of 0.5 cm/min was applied. Subsequently, the static trapped gas phase was recorded by μ-CT to measure the gas phase distribution. To ensure that the trapped gas phase is static, i.e., no bubble movement and no dissolution into the air-saturated water phase occur; we conduct a long-term experiment and measured the volumetric gas content and the total gas surface area with μ-CT after 20 min, 3 h, and 24 h. Both the total gas surface area and

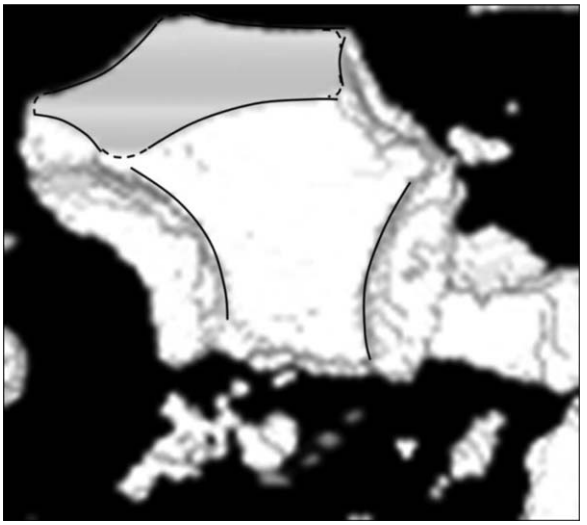

Figure 4. High-resolution (25 μm) CT-image of a trapped gas bubble within 1 mm glass beads. Shown is a horizontal cut through the gas bubble, which indicates five convex curvatures.

the volumetric gas constant are constant during the experiment and the relative standard deviation (SDV) $<2\%$ and $<1\%$, respectively. The constant total gas surface area indicates no gas bubble movement, since a new bubble configuration will exhibit in general another total gas surface area (experimental data are listed in supporting information Text S5).

The device used in this study is an industrial X-ray scanner with a focal spot of 5 μm (X-Tek HMX225). Objects are rotated in a cone beam (135 keV, 633 μA), and projections are recorded on a CCD-Detector Panel with a resolution of 1024 $\times$ 512 pixels. Reconstruction of the data was done with the X-Tek CTPro software package. Important for our experiments is the spatial resolution, since it determines to which lower spatial threshold we can detect trapped gas bubbles. From simple regular cubic- and face-centered packing, one can estimate the following mean pore diameter $d_{k,max} = 0.56$ mm [for details, see *Geistlinger et al*., 2006]. The resolution of the CT-image, i.e., the voxel size has to be somewhat smaller than this diameter that is assumed to reflect the lower threshold of stable gas bubbles. In fact, the spatial resolution of our CT-images was 0.084 mm. In this case, a trapped gas bubble with a diameter of 0.56 mm can be represented by about 157 voxels, i.e., 6–7 voxel along the diameter.

3.2. Image Processing

A 3-D reconstructed CT-image can provide an intuitive impression of the gas phase distribution. To quantify the gas phase distribution, the three different phases, solid, water, and gas, need to be separated. Then, characteristics such as global and local gas saturation, global and local surface of the gas phase, and bubble-size distribution can be determined. Figure 5 shows a 3-D slice of the gas phase after a WT-rising at a rate of 0.6 cm/min indicating trapped gas bubbles of different sizes; e.g., small bubbles that are be trapped within single macropores and large gas bubbles or gas clusters that have a characteristic length scale of few grain diameters. The experimental porosity will be used as a constraint for testing the preceding segmentation procedure discussed below.

First, the 3-D reconstructed images need to be processed in an appropriate manner to enhance the contrast and the boundaries (= edges) between the different physical phases; in our case gas, water, and solid. For the segmentation of the different phases denoising and edge enhancement is essential [*Schlueter et al*., 2010, 2014]. Noise removal was achieved by *total variation* denoising. The L^1-norm for least square criteria is usually avoided, because its variation produces singular expressions. However, as *Rudin et al*. [1992] proofed, noise reduction is more efficient using an L^1-norm objective function instead of an L^2-norm objective function. The *total variation* (TV) of an N-point, piecewise constant signal $\boldsymbol{u}(n)$, $1 \leq n \leq N$ is defined as

$$TV(\boldsymbol{u}) = \sum_{n=2}^{N} |u(n) - u(n-1)| = \|\boldsymbol{Du}\|_1, \tag{1}$$

where $\|\|_i$ denotes the L^i-norm. For the original intensity gray level vector

$$\boldsymbol{f} = \boldsymbol{u} + \boldsymbol{n}, \tag{2}$$

where $\boldsymbol{u}$ is the desired image vector and $\boldsymbol{n}$ the noise vector, the TV-objective function for the denoising algorithm is given by

$$J^*(\boldsymbol{u}) = \|\boldsymbol{Du}\|_1 + \lambda \cdot \|\boldsymbol{f} - \boldsymbol{u}\|_2^2, \tag{3}$$

where the first term minimized the total variation of the image while the second minimized the differences between the original image $\boldsymbol{f}$ and the resulting image $\boldsymbol{u}$. λ denotes the regularization parameter [for details, see *Selesnick and Bayram*, 2010; *Kaestner et al*., 2008; *Burger et al*., 2006]. Small λ-values (<1) results in high regularization, i.e., less noise, and larger λ-values (>1) results in high fidelity to the original image $\boldsymbol{f}$. The only fitting parameter we used in the segmentation process was λ. We found that $\lambda = 10$ gives the best agreement to the porosity constraint (relative errors: column 4 of Table 1; we note that for experiments 7, 8, 9 the porosity constraint is nearly satisfied). The output is a denoised image with nearly uniform distribution of the gray value distribution within each phase. To enhance the phase boundaries, a *Difference-of-Gaussian* filter that works as an unsharp mask was applied. After the preprocessing steps we segmented the trimodal gray-value histogram (see supporting information Text S6) applying the bisegmentation algorithm for each

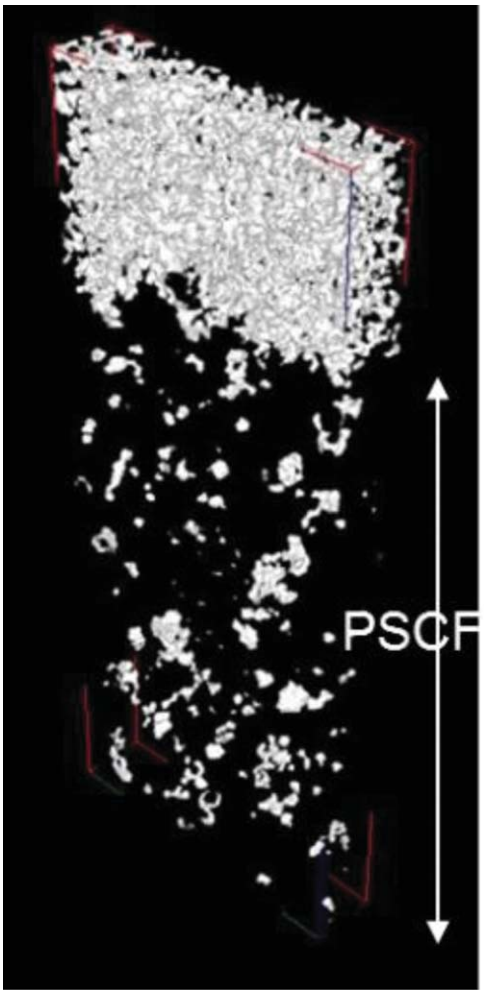

Figure 5. Original CT-image: trapped gas bubbles within the partial saturated capillary fringe after WT rise (0.6 cm/min). The arrow gives the height of the water table rise, i.e., the PSCF.

pair of adjacent phases [for details, see *Vogel and Kretschmar*, 1996]. This algorithm needs a lower and upper threshold indicated in Figure S6 in supporting information Text S6. This thresholding is always a source of subjective errors. We carried out a sensitivity analyses and find out that the results are not sensitive to the lower threshold. The upper threshold was determined by maximizing the entropy of the gray-level distribution of two adjacent phases A and B [*Kapur et al*., 1985]. If $p_1, p_2, \ldots, p_n$ is the probability distribution of the gray-level distribution, the probability distribution for phase A and phase B separated by a gray threshold s is given by $p_1, p_2, \ldots, p_s$ and $p_{s+1}, p_{s+2}, \ldots, p_n$, respectively, where the subspace probability distributions are renormalized. Defining the Boltzmann entropy for each probability distribution

$$S(\pi) = -\sum p_i \ln(p_i), \quad \pi = A, B, \tag{4}$$

and maximizing the total entropy of the gray-value distribution, yields the upper threshold s for the bilevel segmentation algorithm. We test different methods and found the maximum-entropy algorithm is the most objective algorithm that yields the best agreement to the porosity constraint. The lower threshold for each pair of thresholds (gas-water and water-solid) where chosen at that gray value, where the entropy is 95% of its maximum. As output, binary images for each phase were obtained. The comparison between the original image and the processed image is shown in Figure 6. The quantification of phase properties was carried out using Minkowski functionals [*Vogel et al*., 2010], and the gas-water interfacial area was calculated according to *Dalla et al*. [2002]

$$a_{gw} = (a_g + a_w - a_s)/2, \tag{5}$$

(a_{gw}—specific area of the gas-water interface, a_i—specific surface area of the phase $i = g, w, s$). The labeling method of *Hoshen and Kopelman* [1976] is applied for subsequent cluster analysis. All image processing was done using the *QuantIm*-library (Available online at http://quantim.ufz.de).

4. Results and Discussion

4.1. Gas Content Via WT-Rise Velocity

The results of image processing are presented in Table 1 for two experimental series: first series comprises experiments 1–6 with increasing velocities of water table rise and the second series experiments 7–9 representing repetitions for the same velocity. The corresponding WT-rise velocity in cm/min is given in column 2. The porosities obtained from CT (column 3) are in reasonable agreement (mean relative error 7%) with the experimental value (0.332). The relative error is listed in column 4. It is 10% for the first series of experiments and about 3% for the second series of experiments. The mean volumetric gas content over all experiments is 0.019 and its standard deviation is 0.0036, i.e., 19% of the mean value. This value corresponds to a mean gas saturation of 5.6%. A linear regression of volumetric gas content versus velocity yields a rather weak slope of 0.0085 min/cm and a regression coefficient of 0.14 indicating no systematic dependence of

Table 1. Porosity, Volumetric Gas Content, Total Surface, and Gas-Water Interface Depending on Water Table Rise Velocity

Experiment[a]	WT-Rise (cm/min)	Porosity	Error[b]	Gas Content	a_g (1/mm)	$a_{g,w}$ (1/mm)
1	0.1	0.346	4	0.013 ± 0.001	0.149 ± 0.006	0.124 ± 0.005
2	0.2	0.358	8	0.019 ± 0.002	0.222 ± 0.018	0.182 ± 0.014
3	0.3	0.369	11	0.021 ± 0.002	0.229 ± 0.026	0.189 ± 0.021
4	0.4	0.363	9	0.017 ± 0.002	0.187 ± 0.017	0.155 ± 0.014
5	0.5	0.375	13	0.019 ± 0.002	0.201 ± 0.026	0.167 ± 0.022
6	0.6	0.370	11	0.017 ± 0.002	0.193 ± 0.022	0.162 ± 0.018
7	0.5	0.319	4	0.018 ± 0.001	0.215 ± 0.008	0.178 ± 0.007
8	0.5	0.323	3	0.018 ± 0.000	0.215 ± 0.006	0.179 ± 0.005
9	0.5	0.340	2	0.026 ± 0.001	0.296 ± 0.007	0.244 ± 0.006

[a]Experiments were conducted within two series: series 1: experiments 1–6; series 2: experiments 7–9.
[b]The relative error was calculated as deviation between the theoretical porosity (column 3) and the experimental porosity of 0.332. The errors for the quantities in columns 5–7 were derived from these values multiplying them with the corresponding quantity.

trapped air content on WT-rise velocity. This result contradicts our working hypothesis that the faster the water table rise the more gas will be trapped. We conducted three additional experimental series (0.5 mm glass beads, 2 mm glass beads, and mixed 0.5–1 mm glass beads) and found in all cases no systematic dependence of the gas content on WT-rise velocity.

Certainly, this dependence exists for very small WT-rise velocities of about 1 mm/min. We conduct an experiment with such a small WT-rise velocity and found that the gas content was indeed smaller than 1%. This means the porous system had enough time to reach thermodynamic equilibrium. The results seem to indicate that above a critical threshold velocity (∼0.1 cm/min) kinetics and the local pore structure determine the capillary trapping process. Depending on local pore network, water will invade smaller channels and closed loops are formed before larger pores can be invaded and the host fluid can be displaced. Such closed water loops around an air cluster are uniformly distributed over the whole porous media. The larger the closed loop network, i.e., the larger the trapped gas cluster, the lower the probability that, such a closed loop is formed. We think that the local pore structure and local connectivity is the dominant factor that controls the capillary trapping at least in the considered velocity range. This physical picture can explain why the gas content in the second series of experiments has such a large variation from 0.18 to 0.26 although the WT-rise velocity was kept constant. We believe that any investigation of the trapping efficiency on the capillary number between 2×10^{-7} and 10^{-6} of the invading fluid will give no systematic trend. It is not the capillary number that determines the time for forming a closed loop or snap-off time, but the interfacial tension (i.e., the driving capillary force) and the viscosity of that fluid which determines the movement of the interface; i.e., the fluid with the higher viscosity. Such behavior was reported for CO_2-capillary trapping by *Harper et al*. [2012].

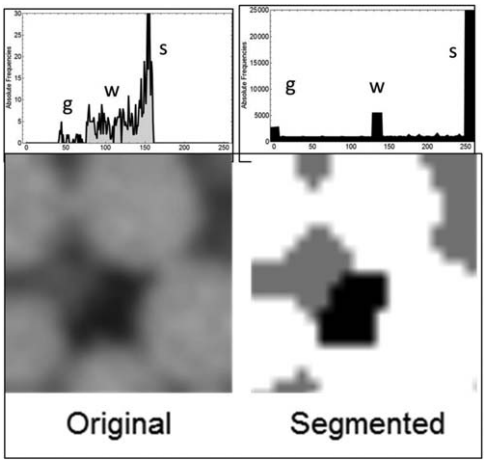

Figure 6. Comparison between the original and the segmented image (white: solid phase, black: trapped gas bubble, gray: water phase). Inserted are the corresponding gray-level histograms. The histogram of the segmented image is given by a three single levels; each representing a certain phase. The broadening is conducted only for better visualization.

4.2. Specific Gas-Water Interface Via Gas Saturation

In columns 6 and 7 (Table 1), the specific gas surface in 1/mm and the specific gas-water interface are presented and its dependence on gas saturation is shown in Figure 7. Figure 7 shows that the specific gas-water interface is about 83 ± 5% of the total gas surface. Both the surface and the gas-water interface show a linear dependence ($R^2 = 0.98$) on gas saturation. This linear dependence was also found by *Pan et al*. [2007] for residual NAPL (Toluene). The NAPL-water interface varies from 0.18 to 0.45 1/mm for a NAPL-saturation range from 4% to 10%. The porous media consists of spherical particles with diameter = 0.68 mm and had a porosity of 0.39.

Our values vary from 0.13 to 0.30 1/mm for the same range of saturation and are about 30% smaller. This is

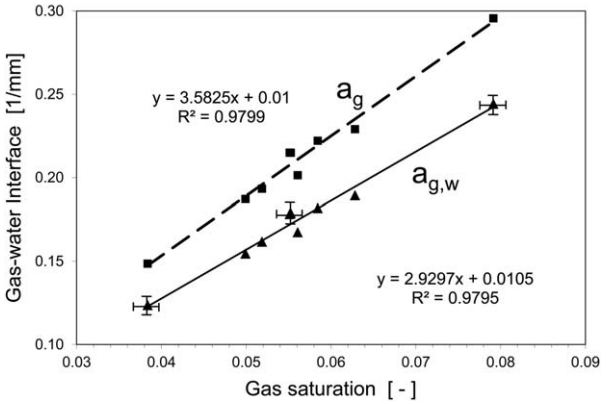

Figure 7. Specific gas surface a_g and specific gas-water interface $a_{g,w}$ via gas saturation. For the gas-water interface, the relative errors are indicated by error bars for data where the porosity constraint is almost satisfied.

a direct consequence of the stronger wetting behavior of a water-NAPL-glass beads system (smaller contact angle, for strict thermodynamic calculation see supporting information Text S2). Hence, the NAPL-water-interface can extend more than the gas-water interface, because of its smaller excess *Free Energy*.

4.3. Cluster Analysis, Bubble-Size Distribution, and Geometrical Shape of Single-Pore-Trapped Gas Bubbles and Multipore-Trapped Gas Bubbles

Next, we want discuss exemplarily the statistics of trapped gas clusters for experiment 7. The cluster analysis for experiments 8 and 9 is provided in the supporting information Text S4. In Figure 8, the histogram of trapped gas clusters in terms of voxel numbers (11–1000 voxel) is shown. We cut off very small objects (<11 voxels), because they are afflicted by noise. The total number of trapped gas clusters within the column volume (= 34 mL) is 3695. There are also super large clusters up to 5000 voxels, but rather sparse. Such a large cluster is shown in Figure 9c. Typically, these large clusters consist of a network of connected pores. The whole histogram is provided in the supporting information Text S3. In Figure 10, the corresponding bubble-size distribution is shown, where we converted the irregular gas clusters into equivalent spherical bubbles with the bubble radius r_b. First, we consider gas bubbles with a radius smaller than $d_{k,max}/2 = 0.28$ mm. Such gas bubbles are trapped within a *single pore* and have a typical shape shown in Figure 9a). The number of *single-pore*-trapped gas bubbles is 1958 that is about 53% of the total number of trapped gas bubbles. However, they only contain 16% of the trapped gas volume.

If we consider *multipore*-trapped gas bubbles shown in Figure 9b with a radius between $d_{k,max}/2$ and the grain radius $r_k = d_k/2 = 0.44$ mm, then the number of such bubbles is 1367, i.e., 37% of all trapped gas bubbles. The corresponding gas volume amounts 40%. Although 90% of all trapped gas bubbles are smaller than a grain, they contain only 56% of the total gas volume. The remaining half of the gas volume is trapped by large gas clusters and network-like gas clusters shown in Figure 9c.

It is instructive to compare the derived gas-cluster size distribution of a strongly water-wet three-phase system with the $scCO_2$-cluster size distribution of a weaker water-wet three-phase system that is shown in *Iglauer et al*. [2011, Figure 4]. First, consider the amount of nonwetting phase trapped by single pores. As *Iglauer et al*. [2011] stated one pore volume corresponds approximately to a cluster size of about 30 voxels. At this cluster size the total residual $scCO_2$-phase is almost reached, i.e., the single-pore contribution is negligibly and certainly smaller than 5%. Hence, the contribution of trapped *single-pore* clusters is significantly smaller than in the strongly water-wet three-phase system, where it is about 16%. Second, we compare the contribution of trapped *multipore* clusters. About 50% of the $scCO_2$-phase is trapped by clusters that contain less than 2000 voxel volumes, i.e., less than 70 pore volumes, whereas in the strongly water-wet case about 50% of the residual gas phase is trapped by clusters that contain less than four pore volumes. Consequently, in strongly water-wet

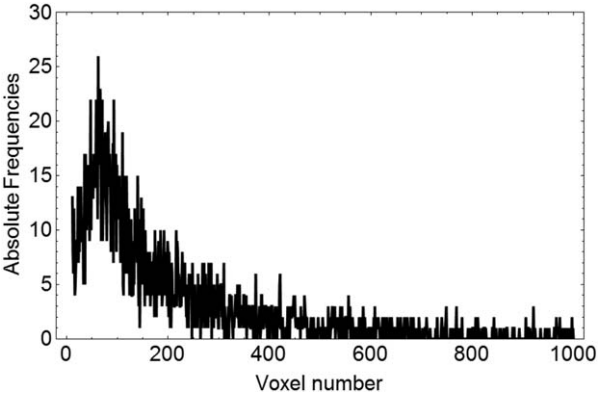

Figure 8. Histogram of isolated gas clusters. Each gas cluster is characterized by its unique voxel number (voxel dimension = 0.083595 mm).

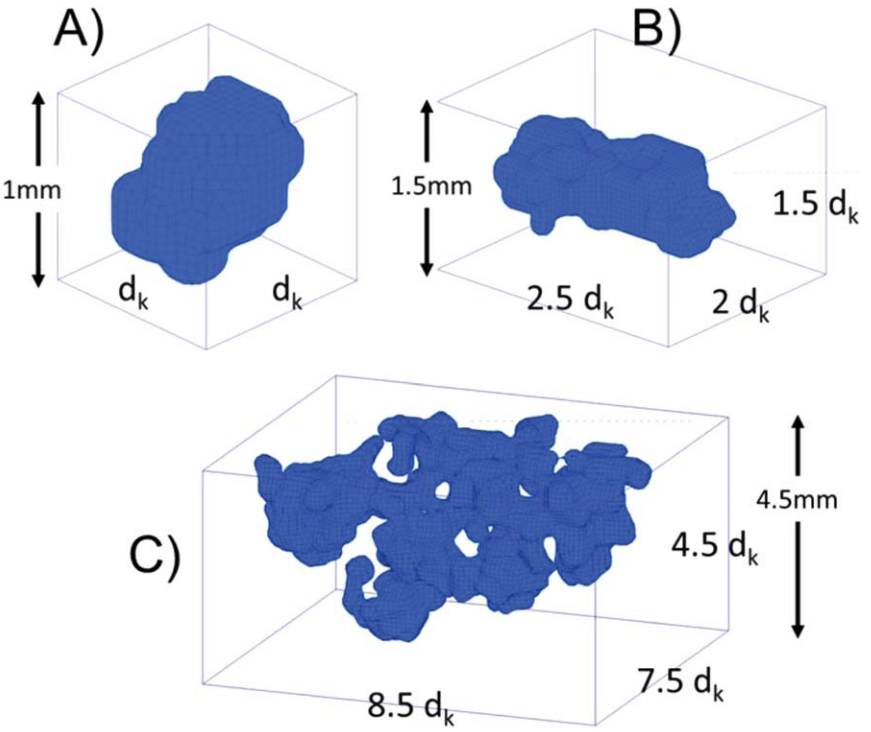

Figure 9. Geometrical shape of a small, medium, and large gas cluster with corresponding voxel numbers (volume in grain volumes) of 152 (0.25), 499 (0.83), 5012 (8.32), respectively.

systems the number and the contribution of smaller trapped gas clusters are significantly larger than in weaker water-wet systems. This result is reasonable, because locally snap-off is suppressed in weaker wet three-phase systems as we discussed above.

The variety of gas clusters of different shape and size has important implications for the bubble-mediated mass transfer, e.g., the dissolution of trapped gas bubbles in the capillary fringe or the dissolution of injected oxygen gas bubbles for groundwater remediation as discussed in *Geistlinger et al*. [2005, 2006]. The key parameter is dissolution rate constant that is given by the product of a mass transfer coefficient and the gas-water interface. Considering the dissolution of trapped oxygen bubbles in a column experiment then the early time behavior of a breakthrough curve (BTC) will be determined by the dissolution of small bubbles (rate constant 1) and the long-time behavior by the dissolution of large bubbles (rate constant 2). That is, half of the area under the BTC is determined by the fast dissolution of the small bubbles and the long tail behavior of the BTC is determined by the slow diffusion of the large bubbles. A dissolution model that assume uniform distributed and equal-sized gas bubbles that is often used in literature (see for details and references *Geistlinger et al*. [2005]) will fail to describe the experimental BTC.

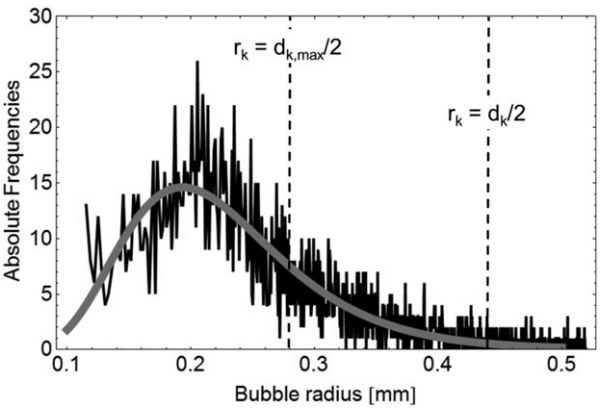

Figure 10. Bubble-size distribution for experiment 7 according to the histogram shown in Figure 8. The solid gray line represents the best fit of a lognormal distribution to the data.

4.4. Bubble-Size Distribution Versus Pore Size Distribution

The key question is, whether the bubble-size distribution shown in Figure 10 exhibits any correlation to the pore size distribution. The experimental pore size

Table 2. Pore Size Distribution: Optimization Results for Normal and Lognormal Distribution

Pore Size Interval (mm)	Relative Frequency	Probability (Normal)	Probability (Lognormal)
<0.1	0.14	0.14	0.08
0.1–0.165	0.38	0.38	0.43
0.165–0.255	0.43	0.43	0.39
>0.255	0.05	0.05	0.11

distribution was obtained from the segmented CT-image using a standard method based on mathematical morphology, i.e., the opening size distribution [*Vogel et al*., 2010]. This algorithm determines the maximum diameter of a sphere, which can be placed inside the pore space at any pore voxel position. This leads to the volume $\boldsymbol{V_i}$ of different pore size classes $\boldsymbol{r_i}$ and the corresponding probability distribution of sphere diameters V_i/*porosity* representing the pore size distribution of the structure. The pore structure was analyzed for four different pore size classes and their relative frequencies $F_{i,i+1}$ listed in Table 2, columns 1 and 2, respectively. We fit two different continuous probability density functions (= pdf(r)) to the relative frequencies: (i) a normal distribution and (ii) a lognormal distribution. Since both functions are two-parameter functions (p_1, p_2) determined by its mean and variance, we have four constraints for two equations. Therefore, we have to solve an optimization problem with the following objective function:

$$F(p_1, p_2) = \sum_{i=1}^{4} \left(P_{i,i+1} - rF_{i,i+1}\right)^2, \tag{6}$$

where

$$P_{i,i+1} = \int_{r_i}^{r_{i+1}} dr \cdot pdf(r).$$

The minimum value of the objective function is 8×10^{-5} for the normal distribution and 0.01 for the lognormal distribution, respectively. Hence, the normal distribution yields a quasi-exact fit, i.e., the resulting probabilities of normal distribution are equal to the relative frequencies (compare columns 2 and 3 of Table 2). The mean pore radius is 0.162 mm and the SDV = 0.057 mm and the corresponding values for the lognormal distribution are: 0.175 mm, 0.063 mm. Both pore size distributions are shown in Figure 11 (black solid curve and black dashed curve). We also show in Figure 11 the heuristic lognormal distribution (gray line) that we estimated from packing configuration: mean radius = r_{mean} = $(d_{k,max} + d_{k,min})/4 = 0.21$ mm, SDV = $d_{k,max}/4 - r_{mean} = 0.07$ mm ($d_{k,min}$ – minimal pore radius).

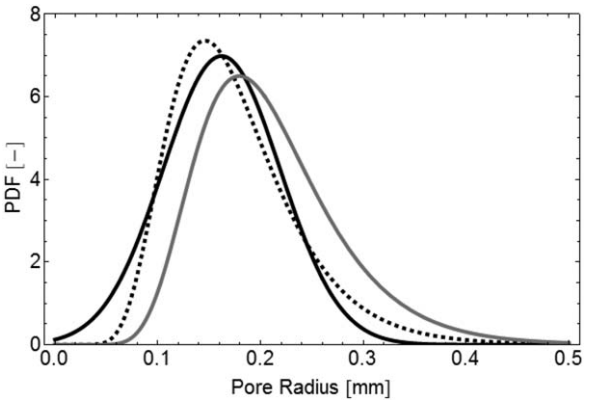

Figure 11. Pore size distribution. Best fits to the experimental, relative frequencies: normal distribution (black solid line), lognormal distribution (black dashed line), and heuristic lognormal distribution (gray line).

The best fit of a continuous lognormal bubble-size distribution to the experimental histogram is shown by the thick gray line in Figure 10 (mean bubble radius = 0.23 mm; SDV = 0.074 mm). In Figure 12, the pore size distribution and the bubble-size distribution are shown. The shadowed regions mark the filled pores for the measured volumetric gas content of 0.018. If the capillary trapping process would be governed by thermodynamics, i.e., by the minimum of the *Free Energy*, then gas is trapped first into large pores and subsequently by smaller pores down to a limiting radius of about 0.3 mm. The comparison

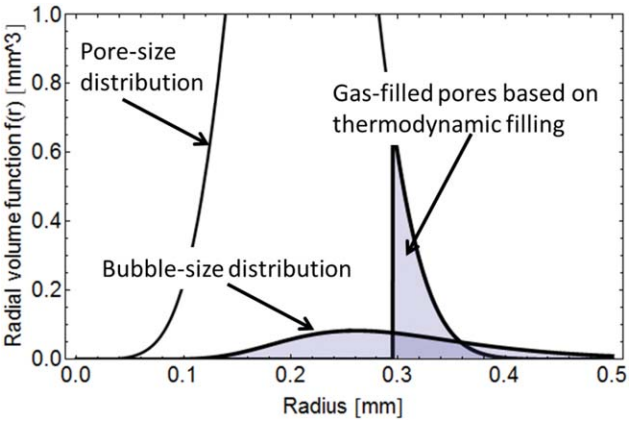

Figure 12. Radial volume f(r) versus radius. Thermodynamical filling of the pore size distribution: pores with radii larger than 0.3 mm are filled with gas bubbles (gray area). Compare it to the realistic bubble-size distribution (= statistical filling).

of the shaded section of the pore size distribution with the shaded area under the bubble-size distribution shows that the process does not reflect thermodynamic equilibrium. A gas bubble will be trapped within a macropore with a probability that is proportional to its occurrence probability i.e., that is proportional to the pore size distribution. Hence, the capillary trapping process is determined by statistics and not by thermodynamics. This is consistent to the findings discussed in section 4.1. Note that this statistical correlation is only valid for a restricted range of the overall histogram shown in Figure 10, i.e., for bubble radii smaller than the grain radius and for front velocities of the invading fluid between 0.1 and 0.6 cm/min.

5. Conclusions

Our study shows that gas can be trapped in single-pores, multipores, and in large connected networks. These large connected clusters can comprise up to eight grain volumes and the sum over such clusters can contain nearly 50% of the whole trapped gas volume. This variety of possible trapped gas clusters of different shape and different volume contradicts the widely accepted picture of *single-pore* trapped gas bubbles. According to our study only 53% of the gas bubbles are trapped in single pores and satisfy the necessary condition of the standard model of capillary trapping, namely that the bubble diameter has to be smaller than $d_{k,max}$. Only for this case it is possible that the bubble is embedded completely by intergranular capillary-held water. For the other 47% trapped gas bubbles, we observed convex-curved gas-solid contact areas indicating thin adsorbed water films. These water films were not directly observable, because of the limited resolution of μ-CT (25 μm).

Since nearly 50% of the gas volume is trapped in gas bubbles larger than the grain diameter this will have consequences on the dissolution behavior. We conclude from our study that models, which assume uniform distributed and equal-sized gas bubbles, will fail to describe the experimental BTC for a gas tracer that originates from the dissolution of trapped gas phases. We conduct a parallel series of dissolution experiments under same experimental conditions like the CT-experiments to study the influence of the nonuniform and heterogeneous bubble-size distribution. The focus of this future work is to study the influence on the BTC on the larger REV scale.

The main conclusion from these findings is that the *multipore behavior* has to be the basis for the derivation of mobility criteria for the onset of bubbly gas flow. Experimental results on discontinuous bubbly flow show that multipore gas clusters of some grain diameter are moving cascade-like upward, if the mobility threshold is reached [*Geistlinger et al.*, 2006].

The most striking and unexpected result was that our *working hypothesis* about the capillary trapping efficiency could not approved. We found no systematic dependence of the gas content on WT-rise velocity. The results seem to indicate that above a certain velocity ($\sim$0.1 cm/min) kinetics and the local pore structure determine the capillary trapping process. We think that the local pore structure and local connectivity is the dominant factor that controls the capillary trapping at least in the considered velocity range. Under these conditions, any investigation of the trapping efficiency on the capillary number of the invading fluid will give no systematic trend. Furthermore, we believe that the relaxation time for establishing thermodynamic equilibrium should be strongly dependent on the time that is needed to displace the nonwetting fluid, i.e., we expect a clear trend of the trapping efficiency on the viscosity of the nonwetting fluid. This physical picture is consistent with finding that the capillary trapping process is determined by statistics and

not by thermodynamics. We found that the bubble-size distribution reflects the pore size distribution for bubble radii smaller than the grain radius.

Based on our pore-scale study, we propose the following settings for continuum multiphase modeling on a REV scale describing capillary trapping by an invading fluid with subsequent mass transfer: in the considered range of front velocities (0.1–0.6 cm/min) the gas saturation is independent of the front velocity and a constant value of about 6% is realistic for 1 mm-GBS or coarse sand. This value has to be estimated for each sediment under consideration. Further work may demonstrate in how far structural attributes as measurable by X-ray-CT can be used to estimate the volume of residual gas. For the calculation of the dissolution rate constant the gas-water interface should be chosen about 80% of the total gas surface and the proposed linear interface-saturation relationship can be applied.

Acknowledgments
The authors gratefully acknowledge funding of the project Dynamically Capillary Fringe (DYCAP) by the German Research Foundation DFG and the Alexander-von-Humboldt Foundation for granting a Feodor-Lynen scholarship to one of the authors.

References

Berg, S., et al. (2013), Real-time 3D imaging of Haines jumps in porous media flow, *Proc. Natl. Acad. Sci. U. S. A.*, *110*, 3755–3759, doi: 10.1073/pnas.1221373110.
Berkowitz, B., S. E. Silliman, and A. M. Dunn (2004), Impact of the capillary fringe on local flow, chemical migration, and microbiology, *Vadose Zone J.*, *3*, 534–548.
Blunt, M. J. (2001), Flow in porous media—Pore-network models and multiphase flow, *Curr. Opin. Colloid Interface Sci.*, *6*, 197–207.
Blunt, M. J., and H. Scher (1995), Pore-level modeling of wetting, *Phys. Rev. E*, *5*, 6387–6403, doi:10.1103/PhysRevE.52.6387.
Brooks, M. C., W. R. Wise, and M. D. Annable (1999), Fundamental changes in in situ air sparging flow patterns, *Ground Water Monit. Rem.*, *19*, 105–113.
Burger, M., G. Gilboa, S. Osher, and J. Xu (2006), Nonlinear inverse scale space methods, *Commun. Math. Sci.*, *4*, 179–212.
Cary, J. W. (1994), Estimating the surface area of fluid phase interfaces in porous media, *J. Contam. Hydrol.*, *15*, 243–248.
Chalbaud, C., M. Robin, J. Lombard, F. Martin, P. Egermann, and H. Bertin (2009), Interfacial tension measurements and wettability evaluation for geological CO_2 storage, *Adv. Water Resour.*, *32*, 98–109, doi:10.1016/j.advwatres.2008.10.012.
Costanza-Robinson, M. S., and M. L. Brusseau (2002), Air-water interfacial areas in unsaturated soils: Evaluation of interfacial domains, *Water Resour. Res.*, *38*(10), 1195, doi:10.1029/2001WR000738.
Dalla, E., M. Hilpert, and C. T. Miller (2002), Computation of the interfacial area for two-fluid porous medium systems, *J. Contam. Hydrol.*, *56*, 25–48.
Derjaguin, B. V. (1940), Tiyra Kapillyarnoy Kondensatsii and drugix Kapillarnvix yavlenii uchetom rasklinivayushchevo daystviya polimolekularnox shidix plenok [in Russian], *Zh. Fiz. Khim.*, *14*, 137.
Donaldson, J. H., J. D. Istok, M. D. Humphrey, K. T. O'Reilly, C. A. Hawelka, and D. H. Mohr (1997), Development and testing of a kinetic model for oxygen transport in porous media in the presence of trapped gas, *Ground Water*, *35*, 270–279.
Dullien, F. A. L. (1992), *Porous Media—Fluid Transport and Pore Structure*, Elsevier, N. Y.
Enouy, R., M. Li, M. A. Ioannidis, and A. J. A. Unger (2011), Gas exsolution and flow during supersaturated water injection in porous media: II. Column experiments and continuum modeling, *Adv. Water Resour.*, *34*, 15–25.
Ezeuko, C. C., and S. R. McDougall (2010), Modeling flow transitions during buoyancy-driven gas migration in liquid-saturated porous media, *Vadose Zone J.*, *9*, 597–609, doi:10.2136/vzj2009.0037.
French, R. H. (2000), Origins and applications of London dispersion and Hamaker constants in ceramics, *J. Am. Ceram. Soc.*, *83*, 2117–2146, doi:10.1111/j.1151-2916.2000.tb01527.x.
Fry, V. A., J. S. Selker, and S. M. Gorelick (1997), Experimental investigations for trapping oxygen gas in saturated porous media for in situ bioremediation, *Water Resour. Res.*, *33*, 2687–2696.
Geistlinger, H., A. Beckmann, and D. Lazik (2005), Mass transfer between a multicomponent trapped gas phase and a mobile water phase: Experiment and theory, *Water Resour. Res.*, *41*, W11408, doi:10.1029/2004WR003885.
Geistlinger, H., G. Krauss, D. Lazik, and L. Luckner (2006), Direct gas injection into saturated glass beads: Transition from incoherent to coherent gas flow pattern, *Water Resour. Res.*, *42*, W07403, doi:10.1029/2005WR004451.
Geistlinger, H., D. Lazik, G. Krauss, and H.-J. Vogel (2009), Pore-scale and continuum modeling of gas flow pattern obtained by high-resolution optical bench-scale experiments, *Water Resour. Res.*, *45*, W04423, doi:10.1029/2007WR006548.
Geistlinger, H., R. Jia, D. Eisermann, and C.-F. Stange (2010), Spatial and temporal variability of dissolved nitrous oxide in near-surface groundwater and bubble-mediated mass transfer to the unsaturated zone, *J. Plant Nutr. Soil Sci.*, *173*, 601–609, doi:10.1002/jpln.200800278.
Glass, R. J., S. H. Conrad, and W. Peplinski (2000), Gravity-destabilized nonwetting phase invasion in macroheterogeneous porous media: Experimental observations of invasion dynamics and scale analysis, *Water Resour. Res.*, *36*, 3121–3137.
Gvirtzman, H., and P. V. Roberts (1991), Pore scale spatial analysis of two immiscible fluids in porous media, *Water Resour. Res.*, *27*, 1165–1176.
Harper, L., and D. Wildenschild (2012), Optimization geological sequestration of CO2 by capillary trapping mechanism, Abstract H21K-05 presented at 2012 Fall Meeting, AGU, San Francisco, Calif.
Herman, B., and J. J. Lemasters (1993), *Optical Microscopy: Emerging Methods and Applications*, Academic, N. Y.
Hilpert, M., and C. T. Miller (2001), Pore-morphology-based simulation of drainage in totally wetting porous media, *Adv. Water Resour.*, *24*, 243–55.
Holocher, J., F. Peeters, W. Aeschbach-Hertig, W. Kinzelbach, and R. Kipfer (2003), Kinetic model of gas bubble dissolution in groundwater and its implications for the dissolved gas composition, *Environ. Sci. Technol.*, *37*, 1337–1343.
Hoshen, J., and R. Kopelman (1976), Percolation and cluster distribution. I. Cluster multiple labeling technique and critical concentration algorithm, *Phys. Rev. B Solid State*, *14*, 3438–3445.
Iglauer, S., A. Paluszny, C. H. Pentland, and M. J. Blunt (2011), Residual CO_2 imaged with X-ray microtomography, *Geophys. Res. Lett.*, *38*, L21403, doi:10.1029/2011GL049680.
Iglauer, S., M. Ferno, P. Shearing, and M. J. Blunt (2012), Comparison of residual oil cluster distribution, morphology and saturation in oil-wet and water-wet sandstone, *J. Colloid Interface Sci.*, *375*, 175–182.

Iglauer, S., A. Paluszny, and M. J. Blunt (2013), Simultaneous oil recovery and residual gas storage: A pore-level analysis using in situ X-ray micro-tomography, *Fuel*, *103*, 905–914.
Joseph, D. D., and Y. Y. Renardy (1993), *Fundamentals of Two-Fluid Dynamics, Part II: Lubricated Transport, Drops and Miscible Liquids, Interdisciplinary Appl. Math. Ser.*, vol. 4, Springer, N. Y.
Juanes, R., E. J. Spiteri, F. M. Orr Jr., and M. J. Blunt (2006), Impact of relative permeability hysteresis on geological CO_2-storage, *Water Resour. Res.*, *42*, W12418, doi:10.1029/2005WR004806.
Kaestner, A., E. Lehmann, and M. Stampanoni (2008), Imaging and image processing in porous media research, *Adv. Water Resour.*, *31*, 1174–1187.
Kapur, J. N., P. K. Shao, and A. K. C. Wong (1985), A new method for gray-level picture thresholding using the entropy of the histogram, *Comput. Vision Graphics Image Process.*, *29*, 273–285.
Kibbey, T. C. G. (2013), The configuration of water on rough natural surfaces: Implications for understanding air-water interfacial area, film thickness, and imaging resolution, *Water Resour. Res.*, *49*, 4765–4774, doi:10.1002/wrcr.20383.
Kovscek, A. R., H. Wong, and C. J. Radke (1993), A pore-level scenario for the development of mixed wettability in oil reservoirs, *AIChE J.*, *39*, 1072–1085.
McCray, J. E., and R. W. Falta (1997), Numerical simulation of air sparging for remediation of NAPL contamination, *Ground Water*, *35*, 99–110.
Melrose, J. C. (1982), Interpretation of mixed wettability states in reservoir rocks, paper SPE 10971 presented at SPE Technical Conference, SPE, New Orleans.
Oostrom, M., M. D. White, and M. L. Brusseau (2001), Theoretical estimation of free and entrapped nonwetting-wetting fluid interfacial areas in porous media, *Adv. Water Resour.*, *24*, 887–898.
Or, D., and M. Tuller (1999), Liquid retention and interfacial area in variably saturated porous media: Upscaling from single-pore to sample-scale model, *Water Resour. Res.*, *35*, 3591–3605.
Oswald, S. E., M. Griepentrog, M. Schirmer, and G. U. Balcke (2008), Interplay between oxygen demand reactions and kinetic gas-water transfer in porous media, *Water Res.*, *42*, 3579–3590.
Pan, C., E. Dalla, D. Franzosi, and C. T. Miller (2007), Pore-scale simulation of entrapped non-aqueous phase liquid dissolution, *Adv. Water Resour.*, *30*, 623–640.
Pentland, C. H., K. Okahabi, T. Suekane, and S. Iglauer (2012), Influence of pore geometry on residual carbon dioxide trapping, paper presented at SPE Asia Pacific Oil & Gas Conference and Exhibition, SPE, Perth, Australia, 22–24 October.
Powers, S. E., C. O. Loureiro, L. M. Abriola, and W. J. Weber (1991), Theoretical study of the significance of nonequilibrium dissolution of nonaqueous phase liquids in subsurface systems, *Water Resour. Res.*, *27*, 463–477.
Radoev, B., K. W. Stöckelhuber, R. Tsekov, and P. Letocart (2007), Wetting film dynamics and stability, *Colloids Interface Sci. Ser.*, *3*, 151–172.
Reeves, P. C., and M. A. Celia (1996), A functional relationship between capillary pressure, saturation, and interfacial area as revealed by a pore-scale network model, *Water Resour. Res.*, *32*, 2345–2358.
Ronen, D., M. Magaritz, N. Paldor, and Y. Bachmat (1986), The behavior of groundwater in the vicinity of the water table evidence by specific discharge profiles, *Water Resour. Res.*, *22*, 1217–1224.
Ronen, D., B. Berkowitz, and M. Magaritz (1989), The development and influence of gas bubbles in phreatic aquifers under natural flow conditions, *Transp. Porous Media*, *4*, 295–306.
Roy, J. W., and J. E. Smith (2007), Multiphase flow and transport caused by spontaneous gas phase growth in the presence of dense non-aqueous phase liquid, *J. Contam. Hydrol.*, *89*, 251–269.
Rudin, L. I., S. Osher, and E. Fatemi (1992), Nonlinear total variation based noise removal algorithms, *Physica D*, *60*, 259–268.
Safran, S. A. (1994), *Statistical Thermodynamics of Surfaces, Interfaces, and Membranes*, 270 pp., Addison-Wesley, Boston, Mass.
Schlueter, S., A. Sheppard, K. Brown, and D. Wildenschild (2014), Image processing of multiphase images obtained via X-ray microtomography: A review, *Water Resour. Res.*, *50*, doi:10.1002/2014WR015256.
Schlueter, S., U. Weller, H.-J. Vogel (2010), Segmentation of X-ray microtomography images of soil using gradient masks, *Computers & Geosciences*, *36*, 1246–1251.
Selesnick, I. W., and I. Bayram (2010), Total variation filtering, Preprint. [Available at http://eeweb.poly.edu/iselesni/lecture_notes/TVDmm/.]
Selker, J. S., M. Niemet, N. G. McDuffie, S. M. Gorelick, and J. Y. Parlange (2007), The local geometry of gas injection into saturated homogeneous porous media, *Transp. Porous Media*, *68*, 107–127, doi:10.1007/s11242-006-0005-0.
Silverstein, D. L., and T. Fort (2000), Prediction of air-water interfacial area in wet unsaturated porous media, *Langmuir*, *16*, 829–834.
Sumner, A. L., E. J. Menke, Y. Dubowski, J. T. Newberg, R. M. Penner, J. C. Hemminger, L. M. Wingen, T. Brauers, and B. J. Finlayson-Pitts (2004), The nature of water on surfaces of laboratory systems and implications for heterogeneous chemistry in the troposphere, *Phys. Chem. Chem. Phys.*, *6*, 604–613.
Tokunaga, T. K. (2011), Physicochemical controls on adsorbed water film thickness in unsaturated geological media, *Water Resour. Res.*, *47*, W08514, doi:10.1029/2011WR010676.
Verwey, E. J. W., and J. Th. G. Overbeck (1948), *Theory of the Stability of Lyophobic Colloids*, Elsevier, Amsterdam.
Vogel, H. J., and A. Kretzschmar (1996), Topological characterization of pore space in soil—Sample preparation and digital image-processing, *Geoderma*, *73*, 23–38.
Vogel, H.-J., U. Weller, and S. Schlueter (2010), Quantification of soil structure based on Minkowski functions, *Comput. Geosci.*, *36*, 1236–1245.
Werth, C. J., C. Zhang, M. L. Brusseau, M. Oostrom, and T. Baumann (2010), A review of non-invasive imaging methods and applications in contaminant hydrogeology research, *J. Contam. Hydrol.*, *113*, 1–24.
Wiesendanger, R. (1994), *Scanning Probe Microscopy: Methods and Applications*, Cambridge Univ. Press, N. Y.
Wildenschild, D., and A. P. Shepard (2013), X-ray imaging and analysis techniques for quantifying pore-scale structure and processes in subsurface porous medium systems, *Adv. Water Resour.*, *51*, 217–246.
Wong, H., S. Morris, and C. J. Radke (1992), Three-dimensional menisci in polygonal capillaries, *J. Colloid Interface Sci.*, *148*, 317–336.